GEOPHYSICS, VOL. 70, NO. 1 (JANUARY-FEBRUARY 2005); P. K12–K19, 8 FIGS.
10.1190/1.1852780

Full-resolution 3D GPR imaging

Mark Grasmueck[1], Ralf Weger[1], and Heinrich Horstmeyer[2]

ABSTRACT

Noninvasive 3D ground-penetrating radar (GPR) imaging with submeter resolution in all directions delineates the internal architecture and processes of the shallow subsurface. Full-resolution imaging requires unaliased recording of reflections *and* diffractions coupled with 3D migration processing. The GPR practitioner can easily determine necessary acquisition trace spacing on a frequency-wavenumber (*f-k*) plot of a representative 2D GPR test profile. Quarter-wavelength spatial sampling is a minimum requirement for full-resolution GPR recording. An intensely fractured limestone quarry serves as a test site for a 100-MHz 3D GPR survey with 0.1 m × 0.2 m trace spacing. This example clearly defines the geometry of fractures in four different orientations, including vertical dips to a depth of 20 m. Decimation to commonly used half-wavelength spatial sampling or only 2D migration processing makes most fractures invisible. The extra data-acquisition effort results in image volumes with submeter resolution, both in the vertical and horizontal directions. Such 3D data sets accurately image fractured rock, sedimentary structures, and archeological remains in previously unseen detail. This makes full-resolution 3D GPR imaging a valuable tool for integrated studies of the shallow subsurface.

INTRODUCTION

Geoscientists, archeologists, and engineers require clear three-dimensional views of the shallow subsurface to see internal geometry and to understand how rock, soil, water, and life interact. High-resolution, nondestructive imaging is needed to reveal the buried historic and geologic record. Compared to imaging for oil/gas reservoir assessment and medical diagnosis, shallow subsurface imaging is still in its infancy.

Recently, 3D ground-penetrating radar (GPR) imaging has provided promising views of the shallow subsurface (Grasmueck, 1996; Beres et al., 1999; Lehmann and Green, 1999; Junck and Jol, 2000; Corbeanu et al., 2001; Szerbiak et al., 2001; Birken et al., 2002; Goodman et al., 2002; Grasmueck and Weger, 2002; Lesmes et al., 2002; Versteeg, 2002; Pipan et al., 2003). The problem is that many of these data sets are spatially aliased, so that a high degree of interpolation is required between parallel profiles. For linear subsurface targets with predictable orientation (e.g., trenches, foundations, utilities, rebars), this may be appropriate. However, complex geologic subsurface features require high-density data acquisition without spatial aliasing of the sampled wavefield. Vermeer (1990) defined the term "full-resolution recording" for unaliased shooting and recording of the seismic wavefield at the basic signal-sampling interval. Here, we introduce the term "full-resolution recording" for unaliased sampling of the electromagnetic wavefield in GPR common-offset measurements. The basic sampling interval allows full reconstruction of the original wavefield. Finer spatial sampling means oversampling; coarser spatial sampling leads to a reduced horizontal resolution and spatial aliasing.

An objective of this paper is to derive quantitative criteria and simple in-field diagnostics for unaliased 3D GPR survey design based on a wavenumber approach (Vermeer, 1990, 2002). The physical justification for full-resolution 3D GPR surveying is confirmed by the real-data example of imaging fractures and joints with millimeter aperture in limestone, which is a challenging imaging task. This demonstrates the potential of full-resolution 3D GPR data sets recorded with a single offset and one antenna polarization.

FULL-RESOLUTION 3D IMAGING

True 3D geometry of the subsurface can be reconstructed from a densely spaced acquisition grid of surface-based coincident source and receiver (zero-offset) wavefield measurements (French, 1974). Three-dimensional migration processing is needed to focus the reflections and diffractions. GPR

Manuscript received by the Editor August 5, 2003; revised manuscript received June 16, 2004; published online January 14, 2005.
[1]University of Miami, RSMAS Marine Geology and Geophysics, 4600 Rickenbacker Causeway, Miami, Florida, 33149. E-mail: mgrasmueck@rsmas.miami.edu; rweger@rsmas.miami.edu.
[2]Swiss Federal Institute of Technology, Institute of Geophysics, ETH-Hönggerberg, CH-8093 Zürich, Switzerland. E-mail: heinrich@aug.ig.erdw.ethz.ch.

receiver antennae have a wide aperture, capturing both vertical and side reflections. The question is, how densely does a 3D GPR survey have to sample the continuous wavefield reaching the surface?

Vertical (time) sampling requirements according to the Nyquist criterion (Nyquist, 1928) can be implemented easily. The sampling interval on the analog-to-digital converter has to be set to less than half the period of the maximum signal and noise frequency content. The resulting vertical resolution can be as small as a quarter-wavelength for vertical separation of distinct features. Isolated, thin horizontal layers and fractures still give a detectable reflection to a thickness of one-fortieth of the signal wavelength (Widess, 1973), or millimeter fracture opening in the case of 100-MHz GPR (Grasmueck, 1996; Lane et al., 2000).

Horizontal (spatial) sampling requirements necessary for optimal imaging and best lateral resolution are more difficult to implement. Spatial sampling translates into GPR measurement spacing in the field. Often, compromises have to be made to keep the acquisition effort at a reasonable level. However, to achieve subwavelength resolution in both the horizontal and vertical directions after 3D migration, full-resolution recording is required (Vermeer, 1990).

THEORETICAL SPATIAL-SAMPLING CONSIDERATIONS

The wavefield response of *any* subsurface geometry can be generated by the superposition of point diffractions (Loewenthal et al., 1976). Migration processing collapses diffraction hyperbolae to their diffraction apices. Therefore, the full-resolution recording requirement for a complex subsurface geometry is to properly sample all diffractions. Trace spacing needs to be dense enough for unaliased sampling of dipping diffraction tails. Derivation of spatial GPR sampling criteria is similar to the seismic zero-offset case shown by Yilmaz (2000, p. 66). Proper sampling of a dipping plane wave requires trace spacing Δx to be equal or smaller than the Nyquist sampling intervals Δx_N,

$$\Delta x \le \Delta x_N = \frac{\lambda}{(4 \sin \alpha)}, \tag{1}$$

where λ is the wavelength and α the dip angle of the plane wave. For constant velocity and horizontal earth surface, the plane-wave angle is equal to the geologic dip of the corresponding plane-reflector element and also equal to the antenna-radiation angle measured from the vertical (Figure 1). For angles of 60° ($\sin 60^\circ = 0.87$) and larger, the spatial Nyquist sampling interval quickly approaches a quarter-wavelength. A diffractor can be approximated by a summation of plane waves with dip angles ranging form 0° to 90°. The rapid increase of maximum dip angle along diffraction hyperbolae, especially for diffractions shallower than 10 m, is demonstrated in Figure 2. This real-data example shows that dip angles of as much as 60° are possible. To maximize focusing and resolution in 3D migration processing, the trace spacing has to be close enough for unaliased sampling of all the energy from a diffraction. Furthermore, GPR antennae have a wide bandwidth with frequency content as much as double the center frequency, or higher. High frequencies and steeply dipping diffraction tails are essential for horizontal resolution (Claerbout, 1976, p. 238). Horizontal resolution after migration is given by

$$\Delta H_r = \frac{\lambda_{min}}{(4 \sin \alpha_{max})}, \tag{2}$$

where ΔH_r is the minimum horizontally resolvable distance, α_{max} is the steepest plane-wave angle used for migration, and λ_{min} is the minimum wavelength observed (Denham, 1981; Ebrom et al., 1995). There is a striking analogy between formulas 1 and 2, directly relating acquisition spacing to achievable horizontal resolution *after* migration processing.

Applying the Nyquist criterion requires the 3D GPR measurements to be spaced in all horizontal directions near a quarter-wavelength of the highest signal and noise frequency content, because diffractions are hyperboloids. The well-known half-wavelength spatial sampling formula (e.g., Sheriff and Geldart, 1995), valid for a seismic spread with one source and multiple receivers, leads to spatially aliased 3D data sets when applied to fixed-offset, single source-and-receiver GPR surveys.

In summary, from a theoretical point of view, the required spatial sampling intervals can be calculated from estimates of minimum wavelength and maximum plane-wave dip. More practical is the method described next, which enables direct estimates of the spatial sampling intervals based on a single 2D test profile.

METHOD TO DETERMINE REQUIRED SPATIAL SAMPLING IN THE FIELD

The frequency-wavenumber (*f-k*) domain is ideally suited for visualizing the sampling of a continuous wavefield emerging from the subsurface (Vermeer, 1990; Blacquiere and Ongkiehong, 2000). It is an excellent tool for survey design and quality control. The method requires collection of a

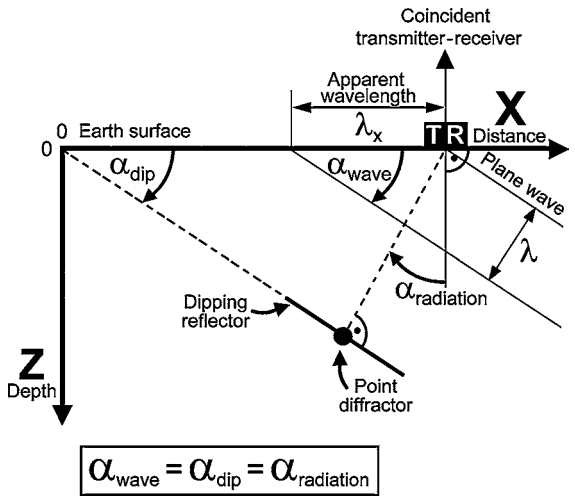

Figure 1. For coincident transmitter-receiver recording geometry with a horizontal earth surface and constant velocity, the plane-wave angle, geologic dip, and radiation angle are all equal. As an approximation, this is also valid for the small transmitter-receiver antenna offsets used in most bistatic constant-offset GPR surveys. Maximum radiation angle of an antenna will, therefore, be directly related to the maximum geologic dip that can be imaged.

densely sampled, representative 2D GPR profile and its transformation into the *f-k* domain. The 2D cross section should sample point diffractions; orientation with respect to geologic dip is less important. A typical *f-k* plot of a 2D GPR profile from a fractured limestone quarry is shown in Figure 3. Both

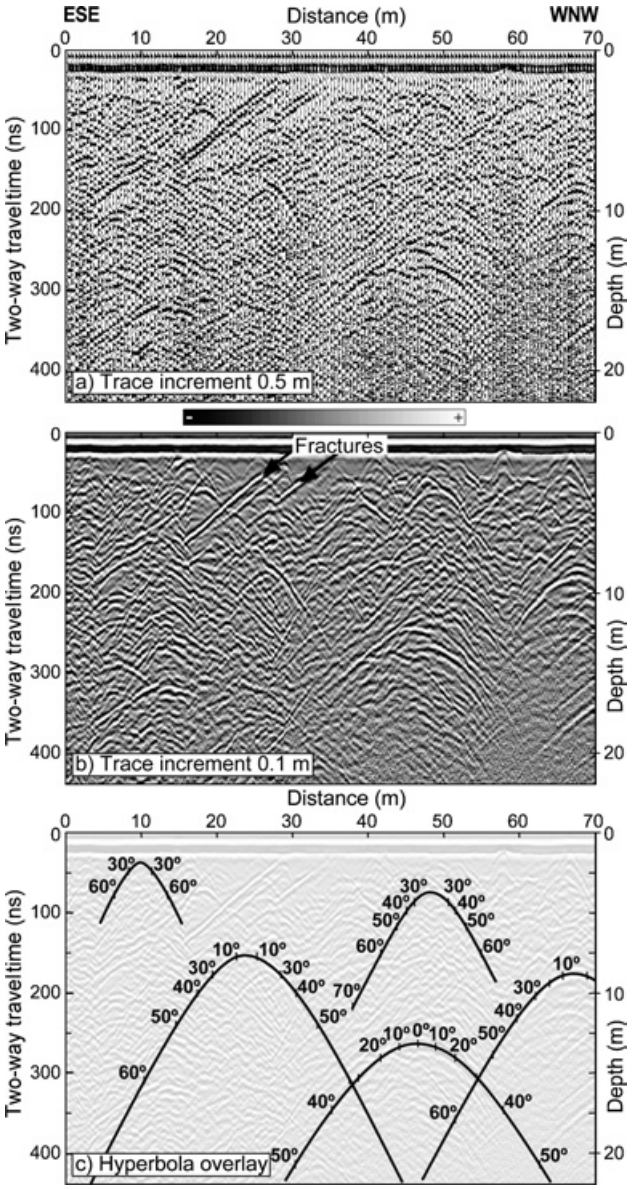

Figure 2. Unmigrated 100-MHz 2D GPR profile from fractured limestone quarry in Callosa, Spain. Ubiquitous diffracted energy from fractures allows no clear definition of fracture and joint geometry. Only two shallow dipping fractures are directly visible. (a) Coarse 0.5-m trace spacing shows aliasing of diffraction tail dips. (b) Dense 0.1-m trace spacing reveals chaotic crisscross patterns from interfering diffraction tails. (c) Superimposed on selected diffraction hyperbolae are geologic dip angles assuming a constant velocity of 0.1 m/ns. As a diffractor can be approximated by a summation of plane waves with dip angles ranging form 0° to 90°, maximum antenna-radiation angles can be inferred from the steepness of the recorded hyperbola branches. For diffractions in less than 10-m depth, diffracted energy has been recorded to angles of 60° and more, necessitating dense trace spacing.

temporal and spatial frequency content can be graphically assessed. Independent of a velocity estimate, the required spatial sampling interval can be directly estimated from the *f-k* plot by transforming k_x values into corresponding Nyquist sampling intervals Δx_N with

$$\Delta x_N = \frac{\lambda_x}{2} = \left| \frac{1}{(2\,k_x)} \right|, \tag{3}$$

where the wavenumber k_x is the inverse of λ_x, the apparent wavelength in x-direction (Figure 1). The definition for k we use here is number of wavelengths per unit distance (Sheriff, 1991, Yilmaz, 2000). With an estimate of a constant ground velocity (e.g., from diffraction analysis or a borehole) and the assumption of a horizontal earth surface, the maximum radiation angle of a GPR antenna over a specific geologic material can be graphically displayed on the *f-k* plot (Figure 3). Equating expressions 1 and 3 delivers the plane-wave dip angle, which is equal to geologic dip and also antenna-radiation angle (Figure 1),

$$\alpha = \arcsin\left(\frac{\lambda k_x}{2}\right). \tag{4}$$

Angles between 60° and 90° are compressed into a narrow sector on the *f-k* plot, again demonstrating the need for near quarter-wavelength spatial sampling. In the case of, e.g., a 0.5-m spatial sampling interval (top of Figure 2), the sector of strong amplitudes in the *f-k* plot would be severely truncated (Figure 3), causing wrap-around (aliasing) effects, irreversibly contaminating the desired signals (e.g., Yilmaz, 2000, p. 64).

The often-practiced method of determining the spatial sampling interval based on maximum geologic dip is problematic. Even if geologic dip is horizontal, reflector terminations and small-scale heterogeneities create diffractions with steep dips. Diffraction tail dip is independent of and always equal

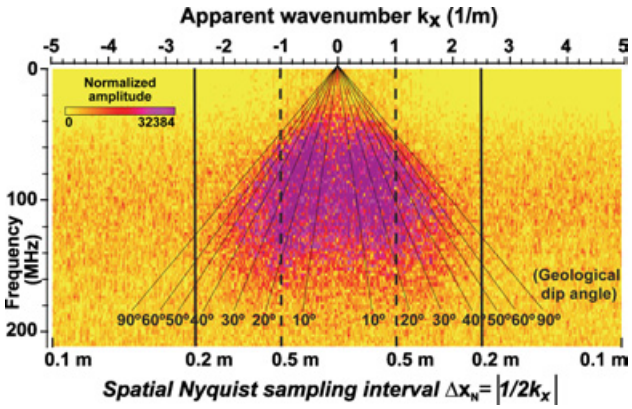

Figure 3. Frequency-wavenumber (*f-k*) plot of 2D GPR profile shown in Figure 2 acquired with 0.1-m trace spacing in fractured limestone quarry. Spatial Nyquist sampling intervals Δx_N can be directly determined from k_x values. In this case, spatial sampling of 0.2 m or less is necessary for unaliased recording of all significant frequency components. Coarser trace spacing of 0.5 m, as per Figure 2a (stippled lines), would severely truncate the signal sector. Horizontal axis is linear in k_x, but not in Δx_N. Angles of dipping events are calculated assuming a velocity of 0.1 m/ns. Events with dips greater than 60° are present. Note the compression of angles in the 60°–90° sectors.

to or steeper than geologic dip (Figure 2). Using a GPR grid spacing larger than a quarter-wavelength in the presence of diffractions not only decreases horizontal resolution, it also creates aliased dipping events, which produce migration artifacts that blur the real events.

Another criterion commonly used to determine GPR survey grid spacing is the diameter of the first Fresnel zone, which determines horizontal resolution as a function of depth in unmigrated GPR surveys. The diameter of the Fresnel zone increases with depth, and corresponding trace spacings are generally too coarse to achieve subwavelength horizontal resolution over the entire depth range.

In summary, if the objective of a 3D GPR survey is to image the shallow subsurface at the best possible resolution, approaching quarter-wavelength both horizontally and vertically, the grid spacing has to be a quarter-wavelength or less of the maximum signal-and-noise frequency measured. In most practical situations, spacing between parallel GPR profiles should be approximately a quarter of the dipole antenna length or less. The maximum antenna-radiation angle should be in the order of 60°, which is the case for most commercial GPR antennae. Worldwide, only a handful of high-resolution geoscientific 3D GPR surveys have been acquired. The primary bottleneck is that it takes days to weeks to acquire a high-density 3D survey the size of two basketball courts (30 m × 30 m). The following real-data example demonstrates that the extra effort to acquire such full-resolution data sets is rewarded with increased data quality.

FIELD EXAMPLE: IMAGING STEEP FRACTURES

To test the capability of 3D GPR to image the geometry of steep, permeable fracture zones, we carried out a survey in a fractured limestone quarry in southeastern Spain, near the village of Callosa, 42 km southwest of the city of Alicante. In outcrop, the fractured, slightly metamorphosed Triassic limestone exposes a complex pattern of fractures with millimeter openings (Figure 4). Original depositional layering and structures are mostly overprinted by metamorphism.

Densely sampled, unmigrated 2D GPR profiles are full of chaotic diffraction patterns with no clear definition of the fracture network (Figure 2). Similar crisscross wave patterns caused by interfering diffraction tails have been discribed by Rieber (1937) on seismic lines crossing fractured zones. Pipan et al. (2003) use crisscross patterns in 2D GPR data as indicators of fractured zones in limestone without a clear image of fracture geometry. The *f-k* analysis of the 2D test line (Figure 3) shows that a minimum spatial sampling interval of 0.2 m is required to capture all significant wave-frequency content. We acquired a full-resolution, 100-MHz 3D GPR data set covering 1000 m^2 in one day with the system developed by Lehman and Green (1999). The grid spacing of radar measurements was 0.1 m × 0.2 m. Transmitter-receiver antenna offset was 1 m. Data processing included drift correction of onset time, removal of low period signal offsets by mean filtering, amplitude decay compensation with the same function applied to all traces, and 40–200-MHz bandpass filtering. The profile in Figure 5, extracted from the middle of the cube, shows an abundance of point diffractions that are evident as circles on horizontal time slices (Figure 6). On time-slice animations (see also http://mgg.rsmas.miami.edu/groups/csl/gpr/), the patterns resemble raindrops falling onto a smooth pond surface. The circular patterns are horizontal cuts through diffraction hyperboloids distributed within the entire data volume.

The constant-velocity, 3D phase-shift time migration (velocity = 0.1 m/ns) from a commercial seismic-processing package removed the diffraction patterns and focused their

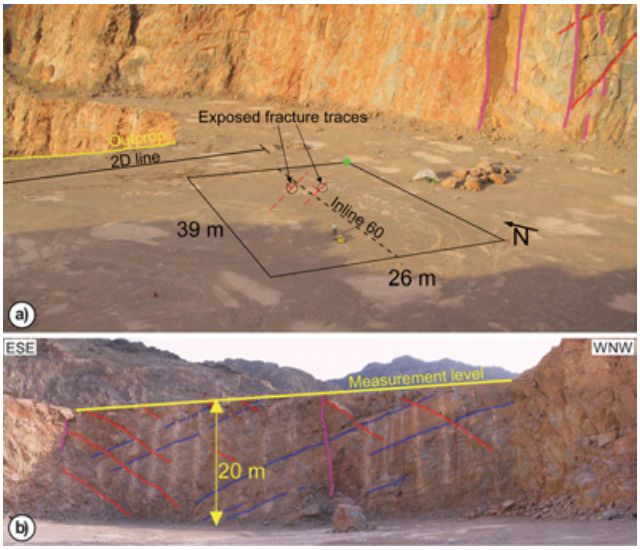

Figure 4. Callosa limestone quarry, Spain: (a) A survey area of 39 m × 26 m was covered with a 0.1 m × 0.2 m, 100-MHz 3D GPR survey in one day. Transmitter-receiver offset was 1.0 m. Data were sampled at 0.8 ns. The 2D test line was used to establish the spatial sampling criteria (Figure 3). On the adjacent outcrop walls, intense fracturing of the rock volume is visible. The orientations of discrete fracture sets are highlighted in color. The color coding is consistent in Figures 4, 6, and 7. (b) The east-southeast–dipping fracture trend (marked in blue) is also visible on the parallel 2D GPR profile (Figure 2). Vertical striations in the lower view are traces of blasting boreholes. The area of the chosen 3D survey was offset more than 25 m from the vertical quarry wall in order to avoid sidewall reflections (Grasmueck, 1996).

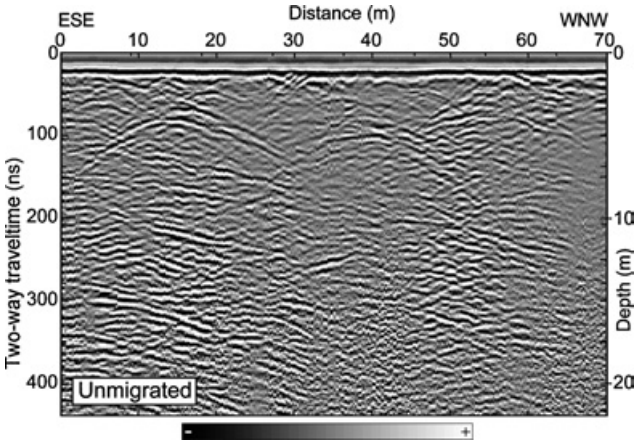

Figure 5. Inline 60 extracted from the middle of the data cube shows an abundance of point diffractions. The profile is plotted with no vertical exaggeration. The same profile is shown in Figure 7 after 3D and 2D migration processing was applied.

energy into fracture signatures. Vertical-fracture images consist of numerous focused diffractions aligned into discrete steep-fracture orientations. Focusing the scattered energy also makes semicontinuous reflections from subhorizontal fractures more traceable. The combination of focused diffractions and properly imaged subhorizontal reflections clearly defines the fracture network within the rock volume. We used rapid interactive animations of 3D subvolumes to interpret and assign elements of four discrete fracture sets (Figure 6 and 7). Animation of consecutive time slices or cross sections visually enhances spatial continuity of fracture orientations. The same fracture sets can be observed in the outcrop (Figure 4). Fractures with millimeter aperture filled with moisture and/or air cause stronger GPR reflections (Lane et al., 2000) and more diffractions. Cemented fractures cause a weaker response. This makes the combination of full-resolution 3D GPR and migration processing a powerful geophysical tool for delineating permeable fracture zones.

DISCUSSION

Detecting steep fractures with no slip requires new imaging approaches

Permeable steep fracture zones can be major fluid conduits. Horizontal stratigraphic flow zones can be interconnected by steep fractures. The probability of detecting steeply dipping permeable zones with vertical boreholes is low. Noninvasive detection of steep fractures with conventional seismic or GPR imaging depends on significant vertical slip, with displacements larger than a quarter-wavelength of intersecting horizontal features (Grasmueck, 1996). Such faults can be highlighted by volumetric coherency attributes enhancing the displacements. Different approaches are needed to image fractures with no slip. Tsoflias et al. (2004) detect vertical fractures by exploiting the polarization properties. Here, we use full-resolution sampling of wide radiation-angle diffractions coupled with 3D migration to image fractured domains in any orientation. In contrast, 2D migration of single GPR profiles produces patterns with no resemblance to the fracture geometry (Figure 7c). Similarly, decimation of the GPR grid spacing from a quarter-wavelength to the more-often-used half-wavelength obscures the circular diffraction patterns on time slices and degrades 3D migration results into uninterpretable chaos (Figure 8).

Diffraction imaging for subwavelength resolution

Diffractions are caused by anomalous bodies smaller than one wavelength, e.g., cavities or boulders. Most densely sampled GPR surveys contain ubiquitous diffracted energy. Crisscross patterns from interfering diffraction tails often are regarded as noise and are suppressed in conventional processing by applying spatial averaging or *f-k* dip filters. Increasing resolution by carefully acquiring and processing the diffractions has also been proposed for seismic imaging (Khaidukov et al., 2003). The origin of diffractions in fractured rock is less

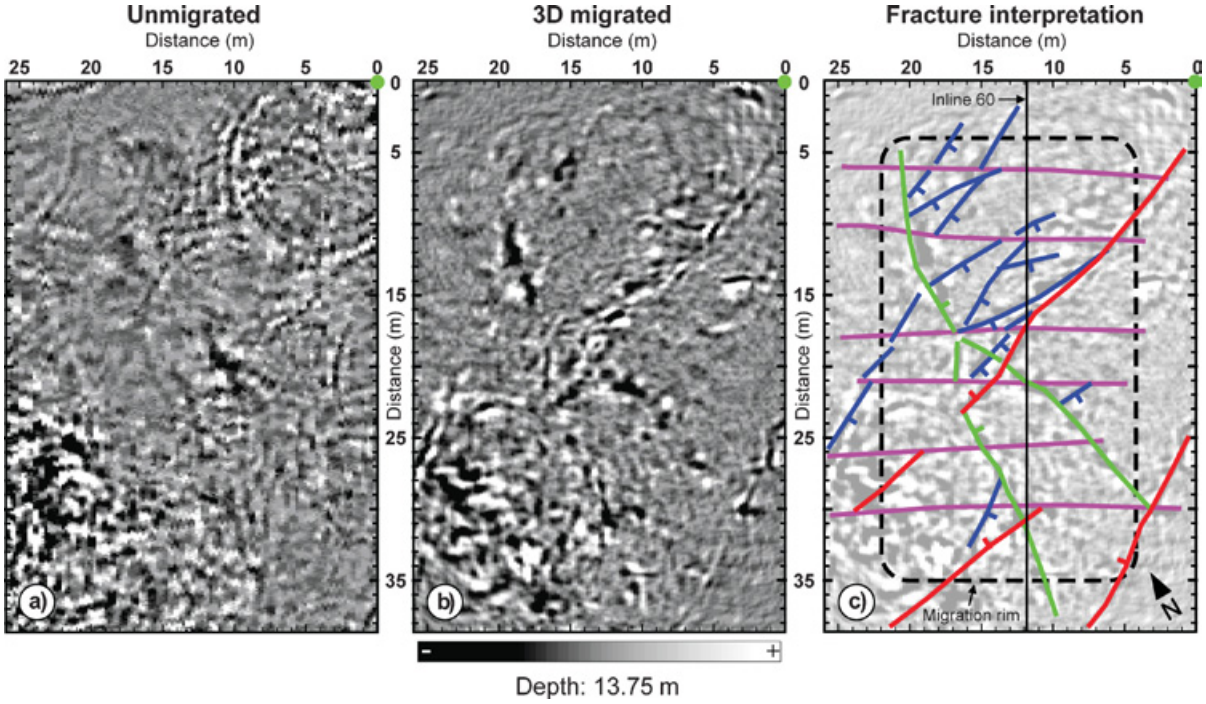

Figure 6. (a) The horizontal slice at 11.0-m depth displays diffraction circles in the unmigrated 3D data set. Graphic pixels correspond to real measurements with no graphic interpolation applied. (b) Phase-shift 3D migration aligns the diffractions into fracture zones. (c) The line-drawing interpretation highlights the four main fracture sets, which also can be observed in the vertical cross section (Figure 7) and in outcrop (Figure 4) with matching color coding. Average dips of the fracture sets are: purple 90°, red 60°, blue 30°, green 30°. Outside the migration rim, not all fracture orientations are clearly imaged. Animated movies optically enhance the visibity of spatial fracture continuity and are viewable at http://mgg.rsmas.miami.edu/groups/csl/gpr/.

understood. In our example, the outcrop displayed very few significant voids related to carbonate dissolution. The many point diffractions in our example must be caused by fractures with millimeter openings, as seen in the quarry walls (Figure 4). Both modeling and field experiments have shown the capability of 100-MHz GPR to detect horizontal fractures with millimeter openings as planar reflections (Grasmueck, 1996; Lane et al., 2000). More investigation, and especially synthetic modeling, is needed to shed light on the origin of point diffractions in fractured rock where joints of different orientations intersect. Ultimately, fracture widths and fill may be quantified.

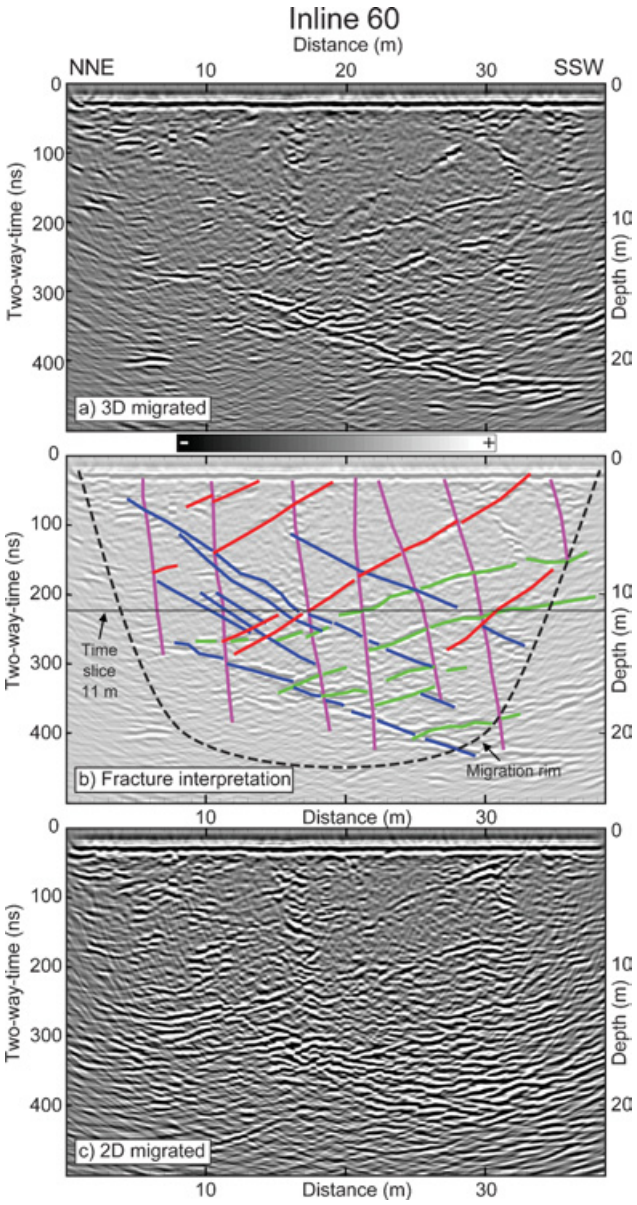

Figure 7. (a, b) The 3D migrated inline 60 displays a complex fracture network with dips from 0° to 90°. Subhorizontal fractures are imaged as plane reflectors, and the subvertical fractures are composed of focused diffraction energy aligned into the fracture zones. Interpretation was aided by rapidly scanning neighboring cross sections to make continuity optically more visible. (c) The 2D migration of inline 60 shows that fracture geometry cannot be extracted from 2D profiles.

Diffractions contain information about the subsurface velocity field

We used centered cross sections of diffraction hyperboloids to determine the migration velocity. Migration-focusing analysis of the many diffraction cones throughout the 3D data volume could be used in new data-adaptive processing schemes to automatically determine velocity-depth models for 3D depth migration, obviating the need to acquire multioffset data. Ellipticity of diffraction patterns on time slices may be an indicator of horizontal anisotropy (Karrenbach, 1990).

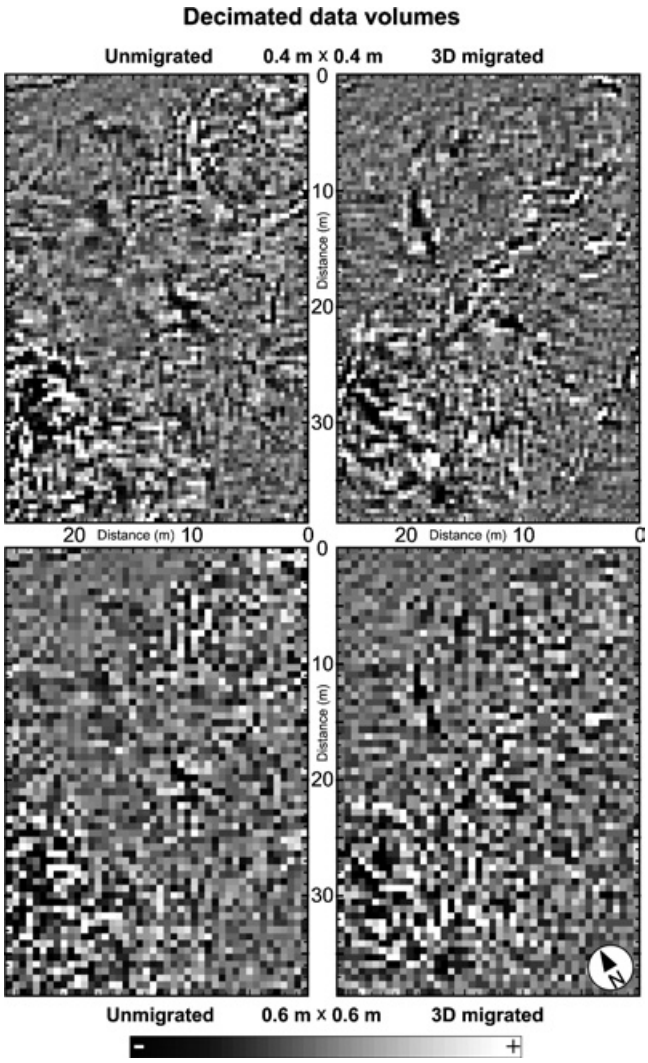

Figure 8. Often-used pseudo-3D surveys, with a coarse grid size of 0.4 m × 0.4 m (top) and 0.6 m × 0.6 m (bottom) simulated by decimation from our full-resolution survey, poorly define diffraction patterns and fractures. Full-resolution spatial sampling at less than a quarter-wavelength is necessary to capture the full diffractions and focus them into clear fracture signatures (see Figure 6).

Full-resolution recording and/or multipolarization acquisition?

Our densely sampled, single polarization survey clearly images a complex fracture network. The circular diffraction patterns observed on horizontal time slices through the unmigrated data volume show that our full-resolution data record diffraction energy originating from all directions. However, far-field modeling of GPR antenna response predicts pronounced directionality (Annan et al., 1975). Lehmann et al. (2000), therefore, proposed to acquire at least two orthogonal 3D surveys, which would double field effort if a single transmitter/receiver system is used. Shallow linear metallic targets (e.g., rebar or utilities) with strong electromagnetic polarization characteristics can be adequately imaged by two sparsely sampled, orthogonal, pseudo-3D surveys (Roberts and Cist, 2002; Annan et al., 2002). Depolarization by subsurface heterogeneity homogenizes the electromagnetic wavefield (Radzevicius and Daniels, 2000). In geologic applications with nonmetallic, complex subsurface geometries, full-resolution 3D imaging with one antenna polarization, as demonstrated by our fracture-imaging example, may be an efficient alternative to acquiring multipolarized but spatially aliased surveys. To test this hypothesis, full-resolution 3D data sets with different antenna polarizations and centimeter-accurate location reproducibility should be acquired and compared. Such experiments would clarify the cases in which multipolarization surveys are needed, as opposed to the more efficient full-resolution single polarization survey shown here. To date, no full-resolution multipolarization 3D GPR survey has been acquired in a geologic setting. Fractured rock would be an ideal natural test setting because of the abundance of point diffractions.

CONCLUSION

Chaotic diffraction patterns from the complex shallow subsurface should not be discarded as noise; instead they should be densely sampled and 3D migrated. Full-resolution 3D GPR imaging requires antennae with a wide-open antenna radiation cone (as much as $\sim 60^\circ$ radiation angle) and at least a quarter-wavelength grid spacing in all directions on the surveying surface. The acquisition of such high-resolution data results in migrated images approaching quarter-wavelength resolution, both in the vertical and horizontal directions. These 3D data sets image fractured rock, sedimentary structures and archeological remains in great detail and provide the basis for geoscientists, archeologists, and engineers to understand the nature and processes of the shallow subsurface. Today's personal-computer technology provides affordable yet powerful resources for 3D processing and visualization. To make full-resolution 3D GPR imaging a widely used, shallow-subsurface assessment tool, the development of more efficient and user-friendly data acquisition systems is needed.

ACKNOWLEDGMENTS

We thank Anya Seward and Guido Bracco-Gartner for their help during acquisition of the dense 3D GPR data. Thanks to Antonio Estévez from the University of Alicante and the operators of the Cantera San Isidoro for arranging and permitting access to the quarry. We are grateful to Alan Green and his group at ETH Zürich for their support in providing the SAGAS field equipment, and for use of their data-processing facility. Promax-3D from Landmark Graphics Corporation was used for 3D migration processing. This work was supported by the Comparative Sedimentology Laboratory at the University of Miami and its industry sponsors, and NSF EAR award #0323213.

REFERENCES

Annan A. P., W. M. Waller, D. W. Strangway, J. R. Rossiter, J. D. Redman, and R. D. Watts, 1975, The electromagnetic response of a low-loss two-layer dielectric earth for horizontal electric dipole excitation: Geophysics, **40**, 285–298.

Annan A. P., S. W. Cosway, and T. DeSouza, 2002, Application of GPR to map concrete to delineate embedded structural elements and defects: International Society for Optical Engineering (SPIE) Proceedings, **4758**, 359–364.

Beres, M., P. Huggenberger, A. G. Green, and H. Horstmeyer, 1999, Using two- and three-dimensional georadar methods to characterize glaciofluvial architecture: Sedimentary Geology, **129**, 1–24.

Birken, R., D. E. Miller, M. Burns, P. Albats, R. Casadonte, R. Deming, T. Derubeis, T. Hansen, and M. Oristaglio, 2002, Efficient large-scale underground utility mapping in New York City using a multi-channel ground-penetrating imaging radar system: International Society for Optical Engineering (SPIE) Proceedings, **4758**, 186–191.

Blacquiere, G., and L. Ongkiehong, 2000, Single sensor recording: Antialias filtering, perturbations and dynamic range: 70th Annual International Meeting, SEG, Expanded Abstracts, 33–36.

Claerbout J. F., 1976, Fundamentals of geophysical data processing: McGraw-Hill Book Co. Inc.

Corbeanu R. M., K. Soegaard, R. B. Szerbiak, J. B. Thurmond, G. A. McMechan, D. Wang, S. Snelgrove, C. B. Forster, and A. Menitove, 2001, Detailed internal architecture of a fluvial channel sandstone determined from outcrop, cores, and 3D ground-penetrating radar; example from the Middle Cretaceous Ferron Sandstone, east-central Utah: AAPG Bulletin, **85**, 1583–1608.

Denham L. R., 1981, Extending the resolution of seismic reflection exploration: Journal Canadian Society of Exploration Geophysicists, **17**, 43–54.

Ebrom D. A., X. H. Li, J. A. McDonald, and L. Lu, 1995, Bin spacing in land 3-D seismic surveys and horizontal resolution in time slices: The Leading Edge, **14**, 37–40.

French W. S., 1974, Two-dimensional and three-dimensional migration of model-experiment reflection profiles: Geophysics, **39**, 265–277.

Goodman, D., S. Piro, and Y. Nishimura, 2002, GPR time slice images of the villa of Emperor Trajanus, Arcinazzo, Italy (a.d. 52–117): International Society for Optical Engineering (SPIE) Proceedings, **4758**, 268–272.

Grasmueck, M., 1996, 3D ground-penetrating radar applied to fracture imaging in gneiss: Geophysics, **61**, 1050–1064.

Grasmueck, M., and R. Weger, 2002, 3D GPR reveals complex internal structure of Pleistocene oolitic sandbar: The Leading Edge, **21**, 634–639.

Junck M. B., and H. M. Jol, 2000, Three-dimensional investigation of geomorphic environments using ground penetrating radar: International Society for Optical Engineering (SPIE) Proceedings, **4084**, 314–318.

Karrenbach, M., 1990, Three-dimensional time-slice migration: Geophysics, **55**, 10–19.

Khaidukov, V., E. Landa, and T. Moser, 2003, Diffraction imaging by a focusing-defocusing approach: 73rd Annual International Meeting, SEG, Expanded Abstracts, 1094–1097..

Lane J. W., M. L. Buursink, F. P. Haeni, and R. J. Versteeg, 2000, Evaluation of ground-penetrating radar to detect free-phase hydrocarbons in fractured rocks—results of numerical modeling and physical experiments: Ground Water, **38**, 929–938.

Lehmann, F., and A. G. Green, 1999, Semiautomated georadar data acquisition in three dimensions: Geophysics, **64**, 719–731.

Lehmann, F., D. E. Boerner, K. Holliger, and A. G. Green, 2000, Multicomponent georadar data: Some important

implications for data acquisition and processing: Geophysics, **65**, 1542–1552.
Lesmes D. P., S. M. Decker, and D. C. Roy, 2002, A multiscale radar-stratigraphic analysis of fluvial aquifer heterogeneity: Geophysics, **67**, 1452–1464.
Loewenthal, D., L. Lu, R. Robertson, and J. Sherwood, 1976, The wave equation applied to migration: Geophysical Prospecting, **24**, 380–399.
Nyquist, H., 1928, Certain topics in telegraph transmission theory: Transactions of the American Institute of Electrical Engineers, **47**, 617–644.
Pipan, M., E. Forte, F. Guangyou, and I. Finetti, 2003, High resolution GPR imaging and joint characterization in limestone: Near Surface Geophysics, **1**, 39–55.
Radzevicius S. J., and J. J. Daniels, 2000, Ground penetrating radar polarization and scattering from cylinders: Journal of Applied Geophysics, **45**, 111–125.
Rieber, F., 1937, Complex reflection patterns and their geologic sources: Geophysics, **2**, 132–160.
Roberts, R., and D. Cist, 2002, Enhanced target imaging in 3D using GPR data from orthogonal profile lines: International Society for Optical Engineering (SPIE) Proceedings, **4758**, 256–261.
Sheriff R. E., 1991, Encyclopedic dictionary of exploration geophysics: SEG.
Sheriff R. E., and L. P. Geldart, 1995, Exploration seismology: Cambridge University Press.
Szerbiak R. B., G. A. McMechan, R. Corbeanu, C. B. Forster, and S. H. Snelgrove, 2001, 3D characterization of a clastic reservoir analog; from 3D GPR data to a 3D fluid permeability model: Geophysics, **66**, 1026–1037.
Tsoflias G. P., J.-P. Van Gestel, P. L. Stoffa, D. D. Blankenship, and M. Sen, 2004, Vertical fracture detection by exploiting the polarization properties of ground-penetrating radar signals: Geophysics, **69**, 803.
Vermeer G. J. O., 1990, Seismic wavefield sampling: Geophysical Reference Series 4, SEG.
Vermeer G. J. O., 2002, 3D Seismic survey design: Geophysical Reference Series 12, SEG.
Versteeg, R., 2002, Near-real time imaging of subsurface processes using geophysics: 72nd Annual International Meeting, SEG, Expanded Abstracts, 1500–1503.
Widess M. B., 1973, How thin is a thin bed?: Geophysics, **38**, 1176–1254.
Yilmaz, O., 2000, Seismic data analysis, *in* M. R. Cooper and S. M. Doherty, eds., Seismic data analysis 1: SEG.